AGU PUBLICATIONS

JGR

Journal of Geophysical Research: Planets

RESEARCH ARTICLE
10.1002/2015JE004799

Key Points:
- Model temperature-time paths for Mount Sharp formation scenarios
- Scenario-dependent predictions in spatial patterns of diagenesis over MSL's path
- Diagenesis is predicted in only some scenarios; temperatures are < 225°C

Correspondence to:
C. S. Borlina,
caue@umich.edu

Citation:
Borlina, C. S., B. L. Ehlmann, and E. S. Kite (2015), Modeling the thermal and physical evolution of Mount Sharp's sedimentary rocks, Gale Crater, Mars: Implications for diagenesis on the MSL Curiosity rover traverse, *J. Geophys. Res. Planets*, *120*, doi:10.1002/2015JE004799.

Received 9 FEB 2015
Accepted 7 JUL 2015
Accepted article online 14 JUL 2015

Modeling the thermal and physical evolution of Mount Sharp's sedimentary rocks, Gale Crater, Mars: Implications for diagenesis on the MSL Curiosity rover traverse

Cauê S. Borlina[1,2], Bethany L. Ehlmann[2,3], and Edwin S. Kite[4]

[1]Department of Atmospheric, Oceanic and Space Sciences, University of Michigan, Ann Arbor, Michigan, USA, [2]Division of Geological and Planetary Sciences, California Institute of Technology, Pasadena, California, USA, [3]Jet Propulsion Laboratory, California Institute of Technology, Pasadena, California, USA, [4]Department of Geophysical Sciences, University of Chicago, Chicago, Illinois, USA

Abstract Gale Crater, the Mars Science Laboratory (MSL) landing site, contains a central mound, named Aeolis Mons (informally Mount Sharp) that preserves 5 km of sedimentary stratigraphy. Formation scenarios include (1) complete filling of Gale Crater followed by partial sediment removal or (2) building of a central deposit with morphology controlled by slope winds and only incomplete sedimentary fill. Here we model temperature-time paths for both scenarios, compare results with analyses provided by MSL Curiosity, and provide scenario-dependent predictions of temperatures of diagenesis along Curiosity's future traverse. The effects of variable sediment thermal conductivity and historical heat flows are also discussed. Modeled erosion and deposition rates are 5–37 μm/yr, consistent with previously published estimates from other Mars locations. The occurrence and spatial patterns of diagenesis depend on sedimentation scenario and surface paleotemperature. For (1) temperatures experienced by sediments decrease monotonically along the traverse and up Mount Sharp stratigraphy, whereas for (2) temperatures increase along the traverse reaching maximum temperatures higher up in Mount Sharp's lower units. If early Mars surface temperatures were similar to modern Mars (mean: −50°C), only select locations under select scenarios permit diagenetic fluids. In contrast, if early Mars surface temperatures averaged 0°C or brines had lowered freezing points, diagenesis is predicted in most locations with temperatures < 225°C. Comparing our predictions with future MSL results on diagenetic textures, secondary mineral assemblages, and their spatial variability will constrain past heat flow, Mount Sharp's formation processes, the availability of liquid water on early Mars, and sediment organic preservation potential.

1. Introduction

Sedimentation processes can provide information on the geologic history of Mars and can constrain the timing of aqueous mineral formation. Such analyses can reveal important information about past habitability, the presence of water at or near the surface of the planet, and potential for the long-term preservation of organic materials. Gale Crater (137.4°E, −4.6°N), the landing site of the NASA Mars Science Laboratory (MSL) mission, is characterized by the presence of a sedimentary stratigraphy, which permits examining ancient Martian environmental conditions and aqueous alteration. The stratigraphic rock record, and thus its geologic history, is preserved in a 5 km high mound called Aeolis Mons (informally, Mount Sharp) within Gale Crater [*Grotzinger et al.*, 2012] (Figure 1a).

Materials comprising Mount Sharp have a low thermal inertia and subhorizontal layers, which together implicate a sedimentary origin [*Pelkey et al.*, 2004; *Anderson and Bell,* 2010; *Thomson et al.*, 2011]. More recent work has suggested that at least some of the lower lying units are cross-bedded sandstones formed by cementation and lithification of sand dunes [*Milliken et al.*, 2014]. The lower mound includes distinctive sedimentary beds containing hydrated sulfates, iron oxides, and Fe/Mg smectite clay minerals, including a distinctive topographic ridge enriched in hematite [*Milliken et al.*, 2010; *Fraeman et al.*, 2013]. Boxwork structures ~1 km above the current crater floor suggest the secondary precipitation of minerals via confined fluid flow through the sedimentary layers [*Anderson and Bell,* 2010; *Thomson et al.*, 2011; *Siebach and Grotzinger*, 2014]. Spectral signatures associated with the upper

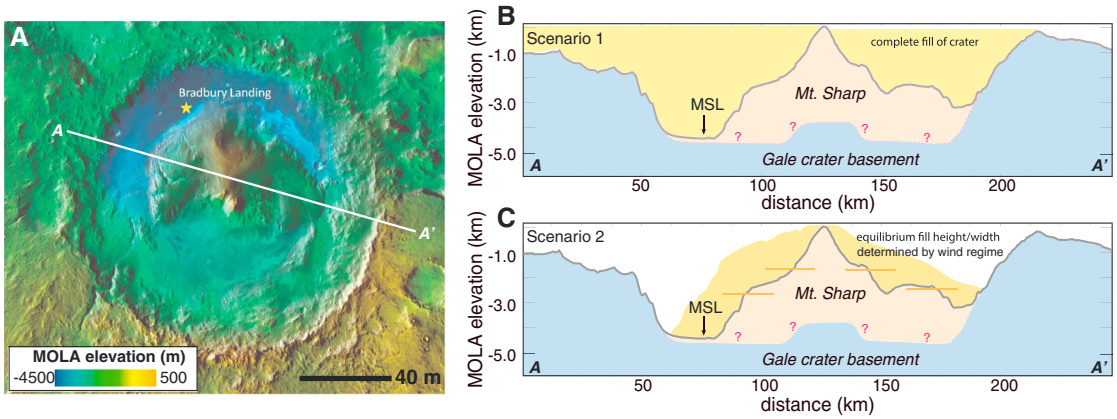

Figure 1. (a) Overview of 154 km diameter Gale Crater (137.4°E, −4.6°N). The star indicates MSL's Bradbury landing site. Aeolis Mons (Mount Sharp) is located on center of the figure. Figure created with Thermal Emission Imaging System (THEMIS) Day infrared integrate with Mars Orbiter Laser Altimeter (MOLA) data sets. Two scenarios for Mount Sharp's formation are analyzed in this paper: (b) complete fill of the crater to the rim, followed by partial exhumation; (c) *Kite et al.* [2013a] model of wind slopes creating feedback with the sides of the crater, enabling mound formation in the center with only incomplete fill.

mound do not permit unique identification of primary or secondary mineral phases either due to their absence or due to dust cover.

Many hypotheses have been developed to explain Mount Sharp formation, variously invoking airfall dust or volcanic ash, lag deposits from ice/snow, aeolian and fluviolacustrine sedimentation (for review, see *Anderson and Bell* [2010], *Wray* [2012], *Le Deit et al.* [2013]). Nevertheless, regardless of the process(es) delivering sedimentary material, two end-member scenarios describe the time evolution, i.e., growth and subsequent erosion, of Mount Sharp. In scenario 1, Gale Crater was completely filled with layered sediments then partially exhumed, leaving a central mound [*Malin and Edgett*, 2000] (Figure 1b). In scenario 2, an aeolian process characterized by slope winds created a wind-topography feedback enabling growth of a high mound without complete fill of the crater [*Kite et al.*, 2013a] (Figure 1c).

The history of Mount Sharp's sedimentation and mineralization provides key constraints on environmental conditions of early Mars, including the availability of liquid water and the nature of geochemical environments. Understanding sediment deposition and possible diagenesis is also crucial to inferring the potential for preservation of organic carbon of biological or abiotic origin, trapped in sedimentary rock strata. Specifically, the thermal history of sediments and their exposure to fluids exerts strong control on the persistence of organic compounds in the sedimentary record [e.g., *Harvey et al.*, 1995; *Lehmann et al.*, 2002]. Initial studies of the diagenesis of Martian sediments [*Tosca and Knoll,* 2009] pointed out the apparent ubiquity of "juvenile" sediments with smectite clays and amorphous silica and a paucity of evidence for illite, chlorite, quartz, and other typical products of diagenesis, which are common in the terrestrial rock record. Thus, a conclusion was that diagenetic processes on Mars were uncommon, perhaps limited by water availability [*Tosca and Knoll,* 2009]. Since then, a growing number of studies have identified clay minerals such as illite, chlorite, and mixed layer clays that commonly form via diagenesis [*Ehlmann et al.*, 2009, 2011a, 2011b; *Milliken and Bish,* 2010; *Carter et al.*, 2013]. So far, minerals identified in Mount Sharp from orbit do not include these phases. However, in situ rover data at Yellowknife Bay imply diagenetic reactions to form mineralized veins, nodules, and filled fractures within the mudstones [*McLennan et al.*, 2014; *Stack et al.*, 2014; *Siebach and Grotzinger*, 2014; *Nachon et al.*, 2014; *Léveillé et al.*, 2014], including exchange of interlayer cations in smectite clays or incipient chloritization [*Vaniman et al.*, 2014; *Rampe et al.*, 2014; *Bristow et al.*, 2015].

Here we model the diagenetic history of sediments comprising Mount Sharp and accessible in rock units along Curiosity's traverse. We couple each of the two sedimentation scenarios [*Malin and Edgett*, 2000; *Kite et al.*, 2013a] with a thermal model for ancient Martian heat flow and timescales for Mount Sharp sedimentary deposition and erosion constrained by crater counts. We model temperature variations experienced within the region between Yellowknife Bay, the base of Mount Sharp, and the unconformity between the lower unit and the upper unit of Mount Sharp and compare them with specific temperature thresholds relevant for diagenesis, e.g., the melting point of water (0°C). We also analyze the time-

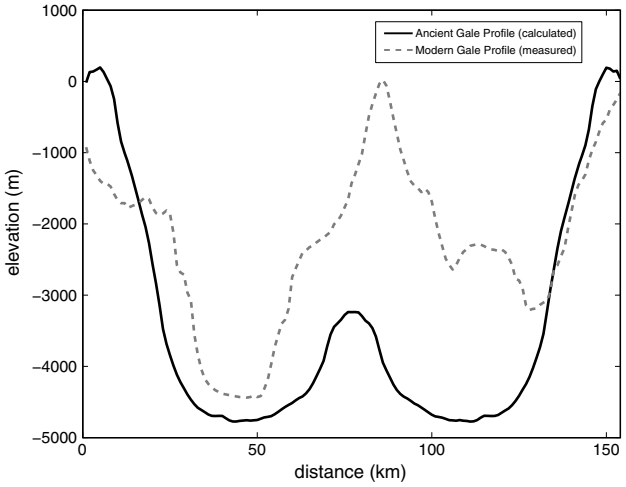

Figure 2. Ancient Gale profile (solid black line) is compared with the modern (dashed gray line) and average (solid gray line) Gale profiles. The ancient Gale profile represents the initial state of the model for every scenario. We model multiple scenarios for how the ancient Gale profile evolved into the modern Gale profile.

temperature integral, an alternative method for predicting mineral stability or instability that takes into account kinetics and is used for predicting the presence or absence of a particular phase, e.g., smectite clays, as described by *Tosca and Knoll* [2009]. Model results are compared to findings obtained by MSL to date and used to draw inferences for sedimentation processes on Mars, their timescales, early Mars temperatures and heat flow, liquid water availability, and the organic preservation potential of Gale sedimentary rocks. Our results on sediment overburden, temperature, and burial timescale also provide crucial input parameters to geochemical models [e.g. *Bristow et al.*, 2015; *Bridges et al.*, 2015], which are constructed to explain the mineralogy of past and future sedimentary rocks examined by Curiosity.

2. Methodology

2.1. Pristine Gale Basement and Modern Topography

In order to trace the evolution of geologic units within Gale Crater, we first established the ancient (starting point) and modern (ending point) topographies of the crater. Gale Crater has been both eroded and filled relative to its original topographic profile (for details, see *Anderson and Bell* [2010]). Consequently, we used empirical fits to Mars Orbiter Laser Altimeter (MOLA) observations of complex craters on Mars to set the initial conditions for Gale Crater's shape, i.e., its initial topographic profile. Observed crater depth-diameter relationships for less modified complex craters on Mars predict a range of initial crater depths for Gale Crater (diameter ~154 km) that goes from 4.2 km to 5.4 km [*Garvin et al.*, 2003; *Boyce and Garbeil*, 2007; *Robbins and Hynek*, 2012]. *Kalynn et al.* [2013] empirically have shown Martian central peak heights of ~1 km for ~100 km craters. Our examination of craters on Mars, better preserved than Gale, with diameters ranging from 131 km to 155 km (at 16°W, 43°S; 36°W, 36°S; 45°E, 42°N) yielded lower bounds on central peak height ranging from 1.0 to 2.1 km that did not scale in a straightforward way with diameter; some may have been influenced by later crater fill. Hence, we set the initial shape of Gale Crater to be 154 km in diameter and 5 km deep with a central peak height of 1.55 km. In order to have realistic central peak heights, and wall slopes, we scaled the average topographic profile from 138 km Moreux crater (45°E, 42°N) to fit Gale's parameters for depth and diameter and generate the starting ancient profile.

There have been suggestions that Gale Crater's central peak height may be near the height of the current topographic high point [*Scott and Chapman,* 1995; *Pelkey et al.*, 2004; *Le Deit et al.*, 2013], i.e., 7X taller than typical central peaks. However, we choose to use a more typical central peak height for the starting topography. The main effect of a higher central peak would be to steepen the bedding orientations predicted in scenario 2 (see below).

Modern Gale Crater has a highly asymmetric central mound, its cross-sectional profile varying with azimuth. Mount Sharp is steeper on the NW, while the southern and eastern portions of the crater have greater amounts of sedimentary fill (Figure 1a). The modern Gale profile shown (Figure 2) was compiled from a roughly NW-SE cross section of present-day crater topography across AA', as seen in Figure 1a. The modern Gale profile is used for estimation of an average overburden, specifically over the Curiosity rover traverse, which is northwest of Mount Sharp (Figure 1).

2.2. Mount Sharp Sedimentation Scenarios

We model two geological scenarios for the time evolution of Mount Sharp filling/removal: (1) complete filling of the crater followed by partial removal leaving a central mound [*Malin and Edgett*, 2000] and (2) slope wind

Table 1. Parameters Employed by *Kite et al.* [2013a, Figure 2b] Compared to Those Used in This Study

Parameters	*Kite et al.* [2013a]	Scenario 2a	Scenario 2b
α	3	3	3
D'	0.4	0.4	Linear variation from $D'_0 = 4$ to $D' = 0$
k_e (erodibility factor)	0.001	0.005	0.01
U_0	0	0	0
R/L	2.4	2.49	2.49

inhibition of complete filling, with mound growth only near the center of the crater and inhibition of sediment accumulation near the sides of the crater by crater-wall slope winds [*Kite et al.*, 2013a].

2.2.1. Scenario 1

Scenario 1 begins with the starting ancient topographic profile and is characterized by complete filling of the crater to the peak of Mount Sharp, followed by partial erosion, leaving the modern profile of Mount Sharp as the final output. Multiple processes are possible to generate this complete fill, including airfall deposition, lacustrine sedimentation, or deposition of lag following snow/ice melt or sublimation. We adopt a simple model of deposition, draping preexisting topography, regardless of geologic process. Which process(es) is at work will influence the character of sedimentary bedding.

Scenario 1 sedimentation and erosion rates depend on the timescales for all models defined in section 2.3. Sedimentation and erosion rates are computed linearly based on the defined model time period and necessary burial/erosion height; i.e., deposition rate is computed as distance from pristine basement to the top of the crater, divided by deposition time. Erosion rate is computed as distance from top of the crater (completely filled crater) to the average modern profile, divided by erosion time.

2.2.2. Scenario 2

Scenario 2 reflects the continuous interplay of sedimentation and aeolian processes where the mound grew close to the center of the crater and the surrounding topography created an environment that generated winds capable of eroding the mound. We use *Kite et al.'s* [2013a] landscape evolution model. In this model a series of approximations are used to determine the balance between the deposition rate D (set at the beginning of each simulation and then held constant during each simulation) and the erosion rate E (time varying). The result is the computation of dz/dt (elevation variation over time) for every time step and is given as

$$\frac{dz}{dt} = D - E. \tag{1}$$

The erosion rate is mainly driven by a power law, which is a function of the magnitude of the shear velocity U,

$$E = k_e U^{\alpha}, \tag{2}$$

where k_e is an erodibility factor and α is a parameter corresponding to aeolian erosion processes such as sand transport, soil erosion, and saltation-induced abrasion. The shear velocity is modeled as the sum of the background bed shear velocity U_0 and the component of shear velocity due to slope winds. The relation is given as

$$U(x) = U_0 + \max\left[\int_x^{\pm\infty} \frac{\partial z'}{\partial x'} \exp\left(\frac{-|x - x'|}{L}\right) dx'\right], \tag{3}$$

where z' is the height, x is the location within the crater ($0 < x < 154$ km, the crater diameter), x' is the distance halfway between the values of x starting at $x = 1.5$ km and ending at $x = 153.5$ km, and L is a correlation length scale [*Kite et al.*, 2013a] (Table 1). At $t = 0$, the basement is represented by a mesh with spacing dx' of unit value.

U and z' both vary (and coevolve) with time. Equation (3) is evaluated for each time step considering winds to the left and right for each location x of 0 to 154 km within Gale Crater. For a given value of x, we compute the integral for left slopes (NW from the central mound; values less than x) and right slopes (SE from the central mound; values greater than x and less than 154 km). The operator *max*[ ] selects the slope with the highest value, which then permits evaluation of equation (2). Equation (1) is also evaluated in each time step,

using E from equation (2) and a value for D determined from the user-set parameter D' ($D = D'E_0$, where E_0 is the average initial erosion rate calculated at the start of the simulation, using the initial topography).

Two sets of parameters that yielded topographic profiles similar to the Gale Crater were used here. Parameters used by *Kite et al.* [2013a] and this study are given in Table 1. We consider two different slope wind model scenarios, designated 2a and 2b. Scenario 2a is defined with a constant deposition rate, set in the first time step of the model as in the *Kite et al.* [2013a] implementation, though a discrete erosion rate is computed in every time step iteration. With our choice of crater wall height, 5 km instead of 10 km in *Kite et al.* [2013a], this led to a thin central mound that does not first grow wide then narrow with erosion like that proposed by *Kite et al.* [2013a] to explain the observed dip of Mount Sharp beds. The scenario 2a mound grows upward with a relatively constant width over time. Consequently, for scenario 2b, we decrease D' linearly with time. This yields results similar to what we see at Gale, e.g., a mound height and shape that matches modern topography and that also steepens with time and retreats back from the wall toward the center, the sequence originally proposed in *Kite et al.* [2013a]. Both scenarios converge on a similar final output although the amount of sediment overburden as a function of time depends on the intermediate steps, i.e., intermediate shape of Mount Sharp.

Because the absolute timescales depend on the erodibility parameter, k_e, which is poorly constrained, we implement timescales in the final output of the model by scaling the output to our specified durations after iterations converged. That is, an evolutionary profile of shape is generated, to which we then assign different potential timescales as described below. All parameters shown in Table 1 are similar to values used by *Kite et al.* [2013a] with the exception of the erodibility parameter (which was tuned until an output similar to Gale Crater width and height was generated), and the functional form of D' in scenario 2b.

2.3. Timescales

Crater counts on the ejecta blanket of Gale Crater constrain its formation age to Late Noachian/Early Hesperian, approximately 3.8 to 3.6 Ga, and place an older age bound on the time period of Mount Sharp deposition [*Thomson et al.*, 2011; *Le Deit et al.*, 2013]. Similarly, a lower limit to the age and extent of lower Mount Sharp can be obtained using the superposition relationship of the topographically lower but stratigraphically higher deposits of Aeolis Palus, which have estimated ages ranging from early Hesperian to early Amazonian [*Thomson et al.*, 2011; *Le Deit et al.*, 2013; *Grant et al.*, 2011], i.e., from ~3.2 to ~3.5 Ga. Thus, most of the formation and erosion of Mount Sharp to its present extent took place during the Hesperian, although processes continued to shape the form of the mound during the Amazonian.

Although surface ages based on crater counts and superposition relationships are useful for relative age dating, pinning in absolute time is challenged by the existence of different chronology models relating the density of craters and time [e.g., *Werner and Tanaka,* 2011]. Numerical ages constraining the start and end of major episodes of Mount Sharp erosion and deposition are required to tie burial history to models of the secular cooling of Mars (section 2.4). Consequently, we examine three different temporal scenarios for the fill and exhumation of Mount Sharp: (1) a standard model, (2) a maximum diagenesis model where deposition is early and exhumation is slow, and (3) a minimum diagenesis model where deposition is late and exhumation is rapid. For (1), Mount Sharp formation begins at 3.7 Ga, reaches 5 km in height, and is then exhumed to reach approximately its present extent by 3.3 Ga. For (2), Gale Crater and Mount Sharp form early, 3.85 Ga, and Mount Sharp is exhumed late, 3.0 Ga, thus providing a maximum for heat flow and duration of burial. For (3), Mount Sharp forms late (3.6 Ga) and is quickly exhumed by 3.4 Ga.

2.4. Thermal Model

The thermal model used here defines temperature as a function of depth and time. We construct it by using the one-dimensional steady state heat conduction solution. The one-dimensional assumption is valid since Mount Sharp is 10 times as wide as it is tall, causing the lateral heat flow to be relatively unimportant for the diagenetic history. For sediments near outer portions of the paleomound, the calculations herein may be considered an upper limit. The steady state assumption is adequate since the Péclet number,

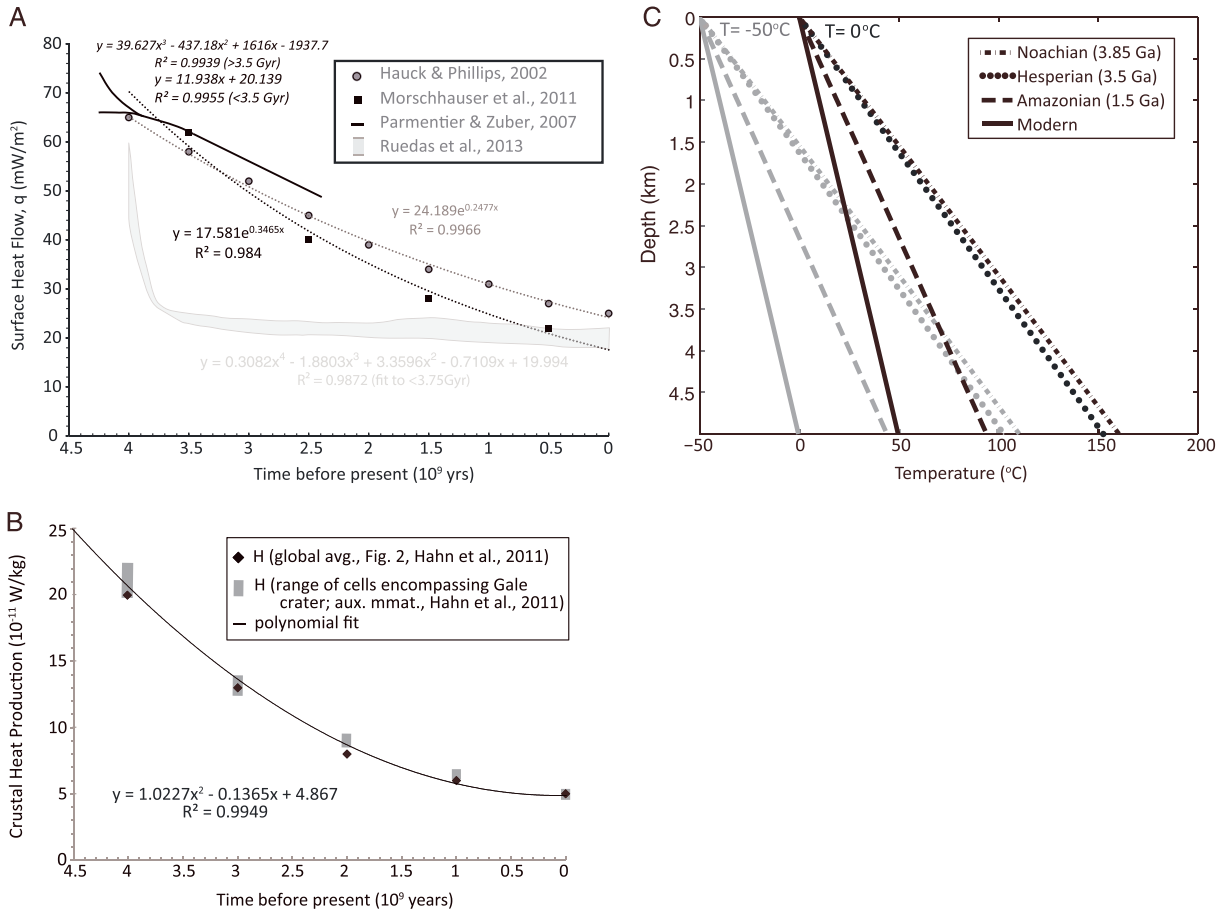

Figure 3. (a) Secular evolution of surface heat flow, $q(t)$, from *Parmentier and Zuber* [2007], *Hauck and Phillips* [2002], *Morschhauser et al.* [2011], and *Ruedas et al.* [2013]. The intermediate Morschhauser et al. model is utilized for the modeling results in subsequent figures. Results of $q(t)$ sensitivity analyses are shown in Table 3. (b) Crustal heat production versus time, $H(t)$, as calculated by *Hahn et al.* [2011b, supporting information] was obtained for the two $5° \times 5°$ grid cells around Gale Crater, averaged, and then fit with a polynomial for straightforward incorporation into the model. The true functional form is a sum of exponentials. Estimated heat production near Gale Crater is similar to estimated global average values. (c) Calculated temperature versus depth relationships for two different mean surface temperatures (0°C and −50°C) as well as four time periods using the models from Figures 3a and 3b along with equation (1).

Pe (deposition or erosion rate, multiplied by deposit thickness, and divided by thermal diffusivity) is $\ll 1$. The temperature T is described as a function of the depth, z, and time, t, as

$$T(z,t) = T_0 + \frac{q(t)}{k}z - \frac{\rho H(t)}{2k}z^2, \tag{4}$$

where T_0 is mean surface temperature, $q(t)$ is the heat flow as a function of time, k is the thermal conductivity, ρ is the density, and $H(t)$ the heat production as a function of time.

2.4.1. Density and Thermal Conductivity

Our baseline values are $\rho = 2500\,\text{kg/m}^3$ and $k = 2\,\text{W/(m °C)}$, values typical for the density of basaltic sandstones and the conductivity of sandstone and claystone rocks on Earth [*Beardsmore and Cull*, 2001]. Since k is dependent on the composition, grain size, and porosity of the sediments, we can also estimate lower and upper bounds to conduct a sensitivity analysis of how choice of k influences Mount Sharp temperature evolution. We set the upper end to correspond to the values of *Hahn et al.* [2011a], $k = 3\,\text{W/(m °C)}$. As a lower end we model $k = 1\,\text{W/(m °C)}$, the lower end of the range for terrestrial shales and also similar to that of gypsum [*Kargel et al.,* 2007].

2.4.2. Early Mars Surface Temperature

The mean surface temperature for early Mars is an unknown. Here we adopt two possibilities: $T_0 = 0$°C and $T_0 = -50$°C in order to analyze how different values of T_0 influence the temperature evolution of sediments. The first presumes a warmer early Mars where temperatures routinely exceed the melting

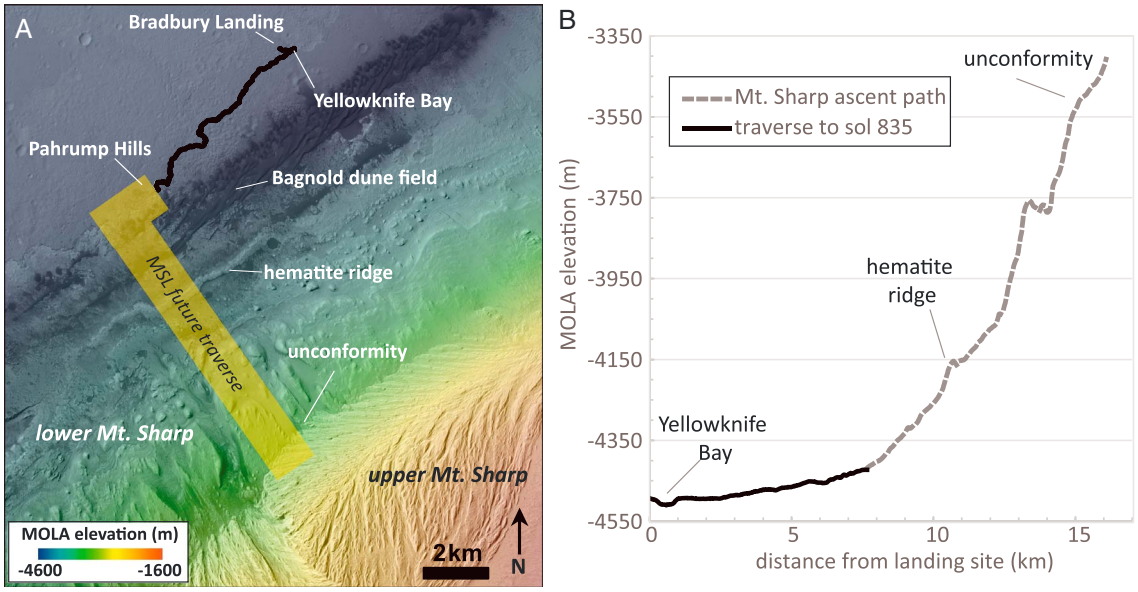

Figure 4. Bradbury Landing, Yellowknife Bay, Pahrump Hills, and potential future MSL locations are identified on the expected traverse region through lower Mount Sharp units. The change in elevation from Yellowknife Bay to the unconformity is ≳1000 m. Yellowknife Bay and Pahrump are at similar radial distances and elevations from Mount Sharp's summit, whereas the unconformity is considerably closer to the central portion of the sedimentary mound and higher in elevation.

point of water during large portions of the Martian year; the latter represents the modern-day average equatorial temperature.

2.4.3. Surface Heat Flow and Crustal Heat Production

The values of $q(t)$ and $H(t)$ were estimated by curve fitting to geophysical models for the evolution of heat flow and crustal heat production, respectively, through time (Figure 3). *Morschhauser et al.* [2011] estimated values for q to be ~60 mW/m^2 at 3.5 Gyr for a variety of cooling scenarios and ~20 mW/m^2 at present. These values are similar to those independently predicted by *Parmentier and Zuber* [2007] and *Hauck and Phillips* [2002], though distinct from the substantially lower lithospheric heat flows predicted by *Ruedas et al.* [2013] and some estimates derived from study of crustal thickness (for review, see *Ruiz et al.* [2011]). Crustal heat production is a function of crustal thickness and the concentration of radiogenic isotopes in the crust. Values calculated by *Hahn et al.* [2011b, Figure 2 and supporting information] (Figure 3b) for the region around Gale Crater are similar to those for average Martian crust. In the scenario modeling results presented, we use *Hahn et al.* [2011b] values for $H(t)$ for all models and *Morschhauser et al.* [2011] for $q(t)$. Figure 3c shows derived temperatures as a function of depth for the two different mean surface temperatures and several time periods, using equation (1). We also report in our sensitivity analyses the effects of different $q(t)$ time evolution models.

Gale may have had additional heating from sources such as residual heat following the Gale-forming impact or local volcanic sources, but we do not include these in our modeling. Were additional sources of heat present, heat flow would be higher and temperatures higher than modeled by burial alone (see section 4).

2.5. Yellowknife Bay to Mount Sharp: Modeling Paleotemperatures on MSL's Traverse

After landing, MSL headed toward Yellowknife Bay, a local topographic low with light-toned sedimentary units. Rocks at Yellowknife Bay preserve evidence for a fluviolacustrine environment [*Grotzinger et al.*, 2014], and several minerals related to aqueous alteration, including Mg smectites and hydrated calcium sulfate, were identified [*Vaniman et al.*, 2014]. Subsequently, the rover has traversed to reach units at the base of Mount Sharp, near a location called Pahrump Hills, and will traverse Murray Buttes, the Bagnold dune field, and continue climbing through stratigraphic units in Mount Sharp (Figure 4).

Given sections 2.1 above, we model the sedimentary and thermal history along the Curiosity traverse, obtained between Yellowknife Bay, the Murray Buttes break in the Bagnold dune field, and predicted future locations of MSL Curiosity. Figure 4 shows Bradbury Landing, Yellowknife Bay, Pahrump Hills, and a

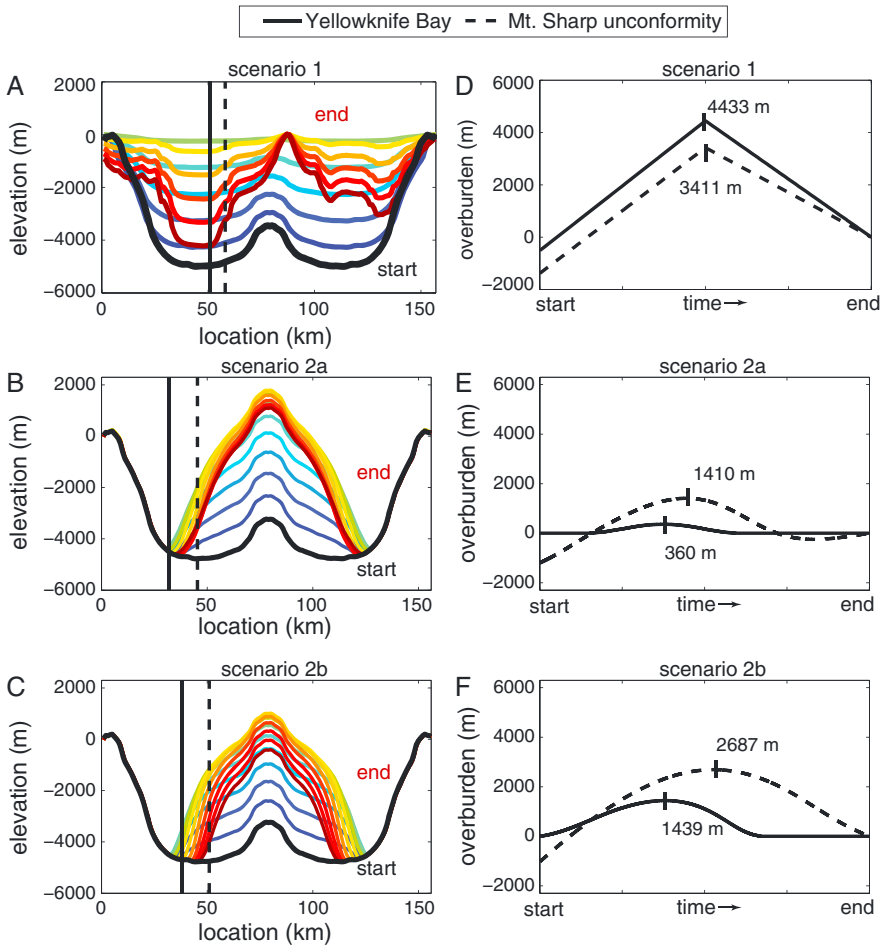

Figure 5. Topography versus time and overburden versus time for (a and d) scenario 1, (b and e) scenario 2a, (c and f) and scenario 2b. Black line shows initial topography, and the colors proceed successively from blue (early stage evolution) stage to red (present-day topography).

potential future path for MSL. We picked the final destination for modeling to be the unconformity marking the boundary between upper and lower Mount Sharp. Upper Mount Sharp may represent a different depositional regime [e.g., *Milliken et al.*, 2010] but likely has slopes too steep to be traversed by Curiosity.

In order to relate model results to rover observations, we compute the ratio between the distance of the closest rim to Yellowknife Bay and the distance of the rim to the foothills of Mount Sharp. This is necessary because different model outputs produce slightly different mound widths, and proper location of the rover relative to the mound is crucial for computation of overburden. The ratio computed is ~0.93. Therefore, for the final output of our models, Yellowknife Bay's location corresponds to 0.93 of the distance between the base of the rim and the foothill of the output mound. Yellowknife Bay and the base of Pahrump Hills (Curiosity's location on Sol 835) have similar rim distances; the elevation at the base of Pahrump is ~60 m higher. The unconformity is set to be at the *x* location that is ~1000 m higher than Yellowknife/Pahrump Hills in the final model output (Figures 4 and 5). Results for the thermal history are subsequently presented as a range of values between Yellowknife Bay and the unconformity in Mount Sharp. This range represents the elevation range along MSL's likely future path. Although approximate, this approach is sufficient to capture the main differences in expected thermal histories for points along MSL's traverse.

2.6. Key Diagenetic Thresholds

After deposition, subsequent fluid circulation through sediments can lead to textural changes as well as alteration of existing minerals and formation of new minerals. Phyllosilicates, sulfates, iron oxides, and

silica phases may form and/or undergo phase transitions. These include the formation of illite or chlorite from smectite, the formation of anhydrite or bassanite from gypsum, the formation of silica and zeolite deposits in vugs, and the formation of cristobalite and quartz from opaline silica phases. It is beyond the scope of this work to track all potential diagenetic transitions (for review, see *Mackenzie* [2005]), which depend upon temperature and time (which we do model) as well as the availability and chemistry of diagenetic fluids and kinetics of the reaction (which we do not treat here). Consequently, we focus on physical parameters and report the overburden and the temperature evolution of the sedimentary rocks, including the temperature maximum and the time-temperature integral, key inputs into any geochemical model of diagenetic processes.

Smectite clays, a type of phyllosilicate formed during the reaction of water with silicates, have been detected from orbit in Mount Sharp units [*Milliken et al.*, 2010], regionally within the watershed of Gale Crater [*Ehlmann and Buz,* 2015], as well as found in situ by the Curiosity rover Chemistry & Mineralogy (CheMin) X-Ray Diffraction (XRD) instrument at multiple traverse locations [*Vaniman et al.*, 2014]. Smectites should be a key tracer of diagnetic history because at elevated temperatures they are no longer a thermodynamically stable phase and instead convert to other phyllosilicate phases like illite or chlorite that lack interlayer water via a series of intermediate reactions to form mixed layer clays like illite-smectite or chlorite-smectite [e.g. *Velde*, 1985]. It was originally believed that conversions of smectite to illite or chlorite began at ~40°C or ~90°C, respectively; however, subsequent work has shown the kinetics, and thermodynamics are more complex than this simple temperature threshold and are strongly influenced by fluid chemistry and time [*Velde*, 1985; *Meunier*, 2005].

We report two thresholds relevant for determining whether smectite and other phases would be expected to have converted to another phase. First, we report temperature and also track relative to a single temperature threshold (0°C) that provides a useful parameterization of water availability for alteration. Aqueous fluids may even be available at lower temperatures due to freezing point depression from dissolved salts. Second, we also compute a time-temperature integral (TTI) and provide thresholds marking smectite instability. In this case, we use TTI thresholds established for the smectite-illite conversion, provided by the terrestrial clay mineral rock record [*Tosca and Knoll,* 2009]. The TTI is calculated such that it is zero for time periods when the sediment temperature is < 0°C and calculated as temperature multiplied by time for those time periods when sediment temperatures are greater than zero. Data on TTI thresholds are well developed for smectite conversion to illite but not to chlorite, although the latter may be more likely on Mars due to potassium availability limits on generation of the former. Nevertheless, the TTI is a key indicator of smectite instability and thus likelihood of transformation to other diagenetic phyllosilicates.

3. Results

3.1. Topographic Evolution and Erosion/Deposition Rates

Figures 5a and 5d show the evolution of topography and overburden for scenario 1, complete fill and exhumation, under the standard timing model. In scenario 1, our simple model of complete filling generates draping, uniform sedimentary layers with the present-day slopes of Mount Sharp generated by later exhumation. Other bedding orientations with variable thicknesses are possible depending on the mode of deposition and its constancy with time. The maximum sediment overburden is 4400 m at Yellowknife Bay and 3400 m at the unconformity under the complete fill scenario.

Figure 5 also shows topography and overburden for scenarios 2a (Figures 5b and 5e) and 2b (Figures 5c and 5f). In scenario 2, the presence of slope winds and topography generate layers that dip away from the central peak. Under the continually thin Mount Sharp overburden of scenario 2a, maximum overburdens at Yellowknife Bay and the unconformity are only 350 m and 1400 m, respectively, whereas these increase to 1400 m and 2700 m under the broad then narrowing sedimentation model of scenario 2b. Notably, the overburden values are highest at Yellowknife Bay for scenario 1 but are highest at the unconformity for scenario 2.

If complete crater filling and exhumation to present-day topography is assumed (scenario 1), with the time period assumed to be equally split into an interval of net deposition followed by interval of net erosion, the average rates of erosion and deposition are 5–22 μm/yr and 9–37 μm/yr, respectively, varying with

Table 2. Scenarios for the Timing of Mount Sharp Formation and Consequent Inferred Rates of Erosion/Deposition Under Different Sedimentation Scenarios[a]

Timing Scenario	Deposition Start (Ga)	Erosion End (Ga)	Calculated Average Net Erosion and Deposition Rates (μm/yr)		Calculated Erosion (*E*)/Deposition (*D*) Rates (μm/yr)					
					Scenario 1		Scenario 2a		Scenario 2b	
			E	*D*	*E*	*D*	*E*	*D*	*E*	*D*
Standard model	3.7	3.3	12	16	11	19	11	11	15	17
Maximum diagenesis	3.85	3.0	6	7	5	9	5	5	7	8
Minimum diagenesis	3.6	3.4	24	31	22	37	21	22	29	35

[a]While the erosion/deposition rates are calculated based on the final output of the models, the average net erosion is calculated iteratively at each time step.

location (Table 2). For scenario 2a average erosion rates fall between 5 and 21 μm/yr, while average deposition rates range from 5 to 22 μm/yr. For scenario 2b average erosion rates are within 7–29 μm/yr while deposition rates range from 8 to 35 μm/yr.

3.2. Temperature

Temperature results are based on coupling the topographic evolution of Mount Sharp with a model for Mars' changing geothermal gradient and a timescale. Figure 6 shows the temperature variation with time for two

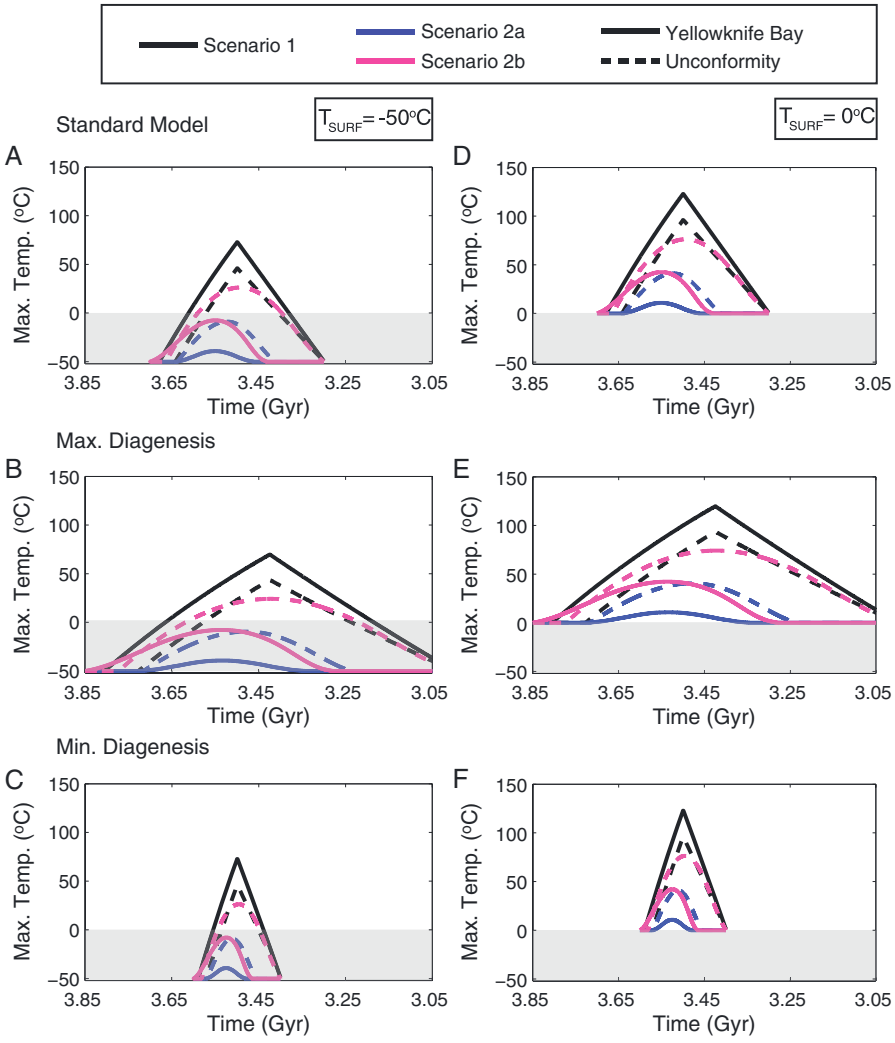

Figure 6. (a–f) Temperature as a function of timing scenarios for scenarios 1, 2a, and 2b considering an early mean surface temperature of either −50°C or 0°C. Solid lines represent location at Yellowknife Bay; dashed lines represent location at the Mount Sharp unconformity.

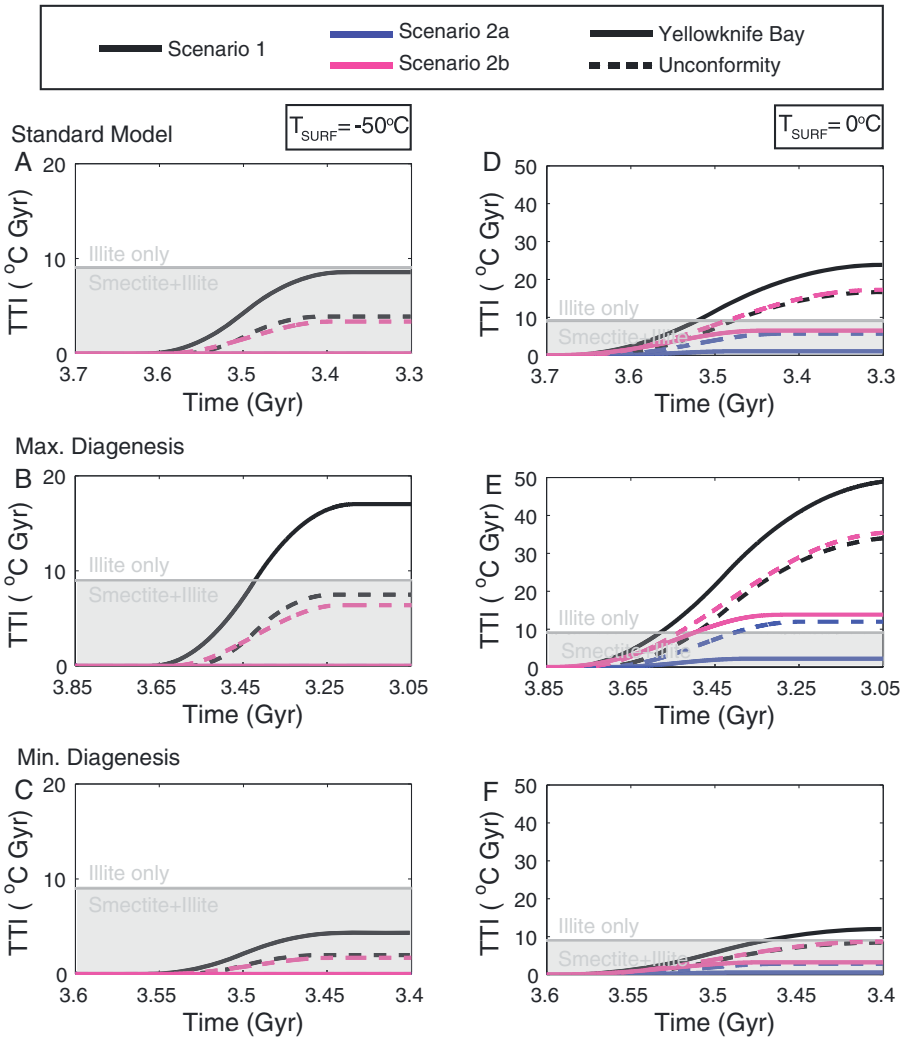

Figure 7. (a–f) Time-temperature integral (TTI) as a function of timing scenarios for sedimentary models 1, 2a, and 2b considering an early mean surface temperature of −50°C and 0°C. Solid lines represent location at Yellowknife Bay; dashed lines represent location at Mount Sharp. As discussed in section 2.6, the TTI should be used as an indicator of smectite instability and transformation, rather than illite stability, because the formation of illite also depends on potassium availability.

locations, i.e., elevations (Yellowknife Bay, solid lines, and the unconformity of Mount Sharp, dashed lines), considering three different timing scenarios and three different sedimentary models. Maximum diagenesis and minimum diagenesis models have the same overall evolution, albeit with slightly different peak temperatures achieved at different points in time.

Figures 6a–6c show results for the different timing scenarios considering a cold early Mars (−50°C), while Figures 6d–6f show results for the same timing scenarios but for a warm early Mars (0°C). In both cases, scenario 1 at Yellowknife Bay produces the highest temperatures of the model (73°C for cold early Mars; 123°C for warm early Mars), while scenario 2a, also at Yellowknife Bay, produces the overall lowest temperatures of the models.

Because we calculate steady state thermal profiles, which is reasonable for the relatively slow erosion and deposition rates summarized in Table 2 ($Pe \ll 1$), and $q(t)$ and $H(t)$ change only modestly over the time periods considered, burial duration and timing has little effect on the peak temperatures achieved and the overall range of temperatures experienced by the sediments. It does, however, significantly affect the time-temperature integral (Figure 7), which is used as a measurement of the expected degree of

diagenesis of smectite clays [e.g., *Tosca and Knoll,* 2009]. Our summary of results below assumes ice or groundwater might be present to cause diagenesis during the duration of burial, an assumption discussed further in section 4.2.

3.2.1. Cold Early Mars

For a cold early Mars, scenario 1 of complete fill predicts subsurface liquid water could occur within Mount Sharp sediments everywhere along the traverse from Yellowknife Bay to the Mount Sharp unconformity. Maximum temperatures reached are ~75°C and ~50°C at Yellowknife Bay and the Mount Sharp unconformity, respectively (Figures 6a–6c). Smectites are expected to be unstable (Figures 7a–7c), though conversion to mixed layer clays would likely be partial, except under the maximum diagenesis timescale.

Scenario 2a, however, does not generate conditions above 0°C for the materials that are currently exposed along MSL's traverse (Figures 6a–6c). Thus, there would be no alteration or diagenesis in situ unless driven by freezing point-depressed salty brines. The cold temperatures would be kinetically challenging for in situ formation of clays. However, importantly, if formed in situ by another process or emplaced as sedimentary detrital clays, scenario 2a implies that smectite clays should be the dominant clay from Yellowknife Bay and Mount Sharp because there are insufficiently high temperatures and time for their conversion to nonswelling forms (Figures 7a–7c).

Scenario 2b predicts liquid water might exist within the upper units of Mount Sharp that could facilitate diagenetic transitions, though temperatures above ~25°C are not reached. However, at Yellowknife Bay the 0°C threshold is not reached, and only freezing point-depressed brines are permitted by the temperature model output, a situation similar to that described for scenario 2a above (Figures 6a–6c). Thus, smectites might be unstable and diagenetically transform to other phyllosilicates in the upper reaches of Mount Sharp, but this conversion is not expected for Yellowknife Bay (Figures 7a–7c).

3.2.2. Warm Early Mars

For warm early Mars, liquid water that might cause alteration and diagenesis could be available everywhere between Yellowknife Bay and Mount Sharp under all scenarios (Figures 6d–6f). In scenario 1, maximum temperatures greater than 100°C occur at both Yellowknife Bay and Mount Sharp. Complete conversion of smectite to more stable phyllosilicates is predicted for all timescales (Figures 7d–7f).

In scenario 2a, maximum temperatures of ~40°C are reached at the unconformity while temperatures at Yellowknife Bay are low, around 15°C (Figures 6d–6f). Consequently, smectites are unstable and expected to convert to other phases near the unconformity, especially for the maximum diagenesis timescale. This is not the case at Yellowknife Bay, and the effects of diagenesis are expected to be minimal under all timescales at that location under scenario 2a, with smectite clays dominating.

In scenario 2b, the maximum temperature at the unconformity is ~75°C and at Yellowknife Bay is ~40°C (Figures 6d–6f). Conversion from smectite to other phases is expected to complete or be nearly complete under standard and maximum diagenesis timescales. Under a minimum diagenesis timescale, little conversion from smectite would be expected at Yellowknife Bay with more possibility for conversion in higher stratigraphic levels of Mount Sharp near the unconformity (Figures 7d–7f).

3.3. Sensitivity Analyses: Surface Heat Flow and Thermal Conductivity

As described in the methodology section, surface heat flow and thermal conductivity are model input parameters that are not fully constrained, so a sensitivity study was conducted in order to analyze the impact of higher or lower ranges in our models (Table 3). Results using the $q(t)$ parameterization from *Parmentier and Zuber* [2007] versus *Morschhauser et al.* [2011] are similar to within 10°C, and the *Hauck and Phillips* [2002] $q(t)$ parameterization would generate results intermediate between the two. *Ruedas et al.*'s [2013] heat flow parameterization predicts considerably smaller values for Noachian Mars to present (Figure 3a), which translate to modeled temperatures tens (at $k > \sim 2$ W/m/K) to hundreds (at $k < \sim 1$ W/m/K) of degrees Celsius lower than the other three thermal models. Because these values are at the extreme lower bounds permitted by Noachian and Hesperian topography [*Ruedas et al.*, 2013, Figure 5], we do not consider further here. Measurements by the upcoming InSight lander mission will soon provide heat flow measurements to help calibrate and discriminate between existing heat flow models.

Table 3. Results of Sensitivity Analyses Using Different Models for the Secular Evolution of Heat Flow, $q(t)$, and Sedimentary Rock Thermal Conductivity (k) as Described in the Text[a]

		Maximum Temperature (°C)/Time-Temperature Integral (°C Gyr)					
		Scenario 1		Scenario 2a		Scenario 2b	
Thermal Conductivity (W/m/K)	Heat Flow	Maximum Temperature	TTI	Maximum Temperature	TTI	Maximum Temperature	TTI
		Yellowknife Bay					
		$T_{surf} = -50$°C					
$k = 1$	*Ruedas et al.* [2013]	36	3	−41	0	−15	0
$k = 1$	*Morschhauser et al.* [2011]	165	49	−28	0	36	3
$k = 1$	*Parmentier and Zuber* [2007]	175	53	−28	0	39	4
$k = 2$	*Ruedas et al.* [2013]	−5	0	−46	0	−33	0
$k = 2$	*Morschhauser et al.* [2011]	73	9	−39	0	−8	0
$k = 2$	*Parmentier and Zuber* [2007]	79	10	−39	0	−6	0
$k = 3$	*Ruedas et al.* [2013]	−27	0	−47	0	−39	0
$k = 3$	*Morschhauser et al.* [2011]	25	2	−43	0	−22	0
$k = 3$	*Parmentier and Zuber* [2007]	29	2	−42	0	−22	0
		$T_{surf} = 0$°C					
$k = 1$	*Ruedas et al.* [2013]	87	16	9	1	34	5
$k = 1$	*Morschhauser et al.* [2011]	215	84	22	2	84	13
$k = 1$	*Parmentier and Zuber* [2007]	225	89	22	2	89	14
$k = 2$	*Ruedas et al.* [2013]	45	9	4	0	17	3
$k = 2$	*Morschhauser et al.* [2011]	123	24	11	1	42	7
$k = 2$	*Parmentier and Zuber* [2007]	129	25	11	1	44	7
$k = 3$	*Ruedas et al.* [2013]	23	5	2	0	10	2
$k = 3$	*Morschhauser et al.* [2011]	75	15	7	1	27	4
$k = 3$	*Parmentier and Zuber* [2007]	79	16	7	1	29	4
		Mount Sharp Unconformity					
		$T_{surf} = -50$°C					
$k = 1$	*Ruedas et al.* [2013]	13	0	−18	0	13	1
$k = 1$	*Morschhauser et al.* [2011]	107	12	29	6	107	39
$k = 1$	*Parmentier and Zuber* [2007]	115	13	37	7	114	43
$k = 2$	*Ruedas et al.* [2013]	−20	0	−34	0	−21	0
$k = 2$	*Morschhauser et al.* [2011]	26	1	−9	0	26	3
$k = 2$	*Parmentier and Zuber* [2007]	30	2	−8	0	30	4
$k = 3$	*Ruedas et al.* [2013]	−33	0	−40	0	−33	0
$k = 3$	*Morschhauser et al.* [2011]	−2	0	−25	0	−2	0
$k = 3$	*Parmentier and Zuber* [2007]	1	0	−22	0	1	0
		$T_{surf} = 0$°C					
$k = 1$	*Ruedas et al.* [2013]	64	10	32	5	63	14
$k = 1$	*Morschhauser et al.* [2011]	157	26	83	24	156	73
$k = 1$	*Parmentier and Zuber* [2007]	165	27	85	25	164	77
$k = 2$	*Ruedas et al.* [2013]	30	5	16	3	30	7
$k = 2$	*Morschhauser et al.* [2011]	76	13	41	7	76	17
$k = 2$	*Parmentier and Zuber* [2007]	80	13	42	7	80	18
$k = 3$	*Ruedas et al.* [2013]	17	3	10	2	18	4
$k = 3$	*Morschhauser et al.* [2011]	48	9	25	4	48	11
$k = 3$	*Parmentier and Zuber* [2007]	51	9	28	4	51	12

[a]Results are reported for Yellowknife Bay and for the Mount Sharp unconformity. The baseline scenario used in all figures is *Morschhauser et al.* [2011] with $k = 2$ W/m/K.

Sedimentary rock thermal conductivity (k) is an important model parameter. Sensitivity analyses show k and the modeled maximum temperature and time-temperature integral (TTI) are inversely related. Low thermal conductivities ($k = 1$ W/m/K) in sedimentary rock lead to up to 150°C higher temperatures than for $k = 3$ W/m/K rocks in scenario 1 at Yellowknife Bay. The difference is less in models and locations with less sedimentary overburden (tens of degrees Celsius) (Table 3).

Terrestrial sedimentary rocks vary widely in thermal conductivity according to grain size and degree of compaction and cementation. Typical values for shales are 1.4–2.1 W/m/K and sandstones 2.8–4.7 W/(m K)

[*Beardsmore and Cull,* 2001]. Loess can have $k = 0.15$ W/(m K) [*Johnson and Lorenz,* 2000], some salt hydrates have $k < 1$ W/(m K) [*Kargel et al.*, 2007], and loosely consolidated, uncemented fine-grained soils can also have $k < 1$ W/(m K) at Mars atmospheric pressures [*Piqueux and Christensen,* 2009]. Placing these values in our model (e.g., $k = 0.25$ W/(m K) produces peak temperatures of 300–1000°C. However, such temperatures are probably unlikely. Overburden causes compaction, which increases grain-to-grain contact points, decreases porosity, and increases thermal conductivity. Furthermore, cementation of pore spaces is common in the presence of waters and diagenesis, increasing thermal conductivity between grains. Calculations by *Piqueux and Christensen* [2009, 2011] show cementing minerals occupying >30% of the pore space of a sedimentary rock with 33% porosity produce thermal conductivities $k > 1$ W/(m °C). Data acquired so far by the Curiosity rover show sedimentary rocks investigated are mostly pore filled [*Grotzinger et al.*, 2014], yet thermal inertia is low [*Martínez et al.*, 2014]. Future heat flow data from InSight along with continued acquisition of surface temperature data by MSL's Rover Environmental Monitoring System and compositional data will allow better estimation of Martian rock thermal conductivity.

4. Discussion

4.1. Martian Deposition and Erosion Rates

Average deposition rate estimates of our model (section 3.1 and Table 2) fall near or within the range of 10–100 μm/yr estimated for deposition of Martian basin-filling, layered sediments called "rhythmites" [*Lewis and Aharonson,* 2014] and the range of 13–200 μm/yr estimated for sedimentation in Aeolis Dorsa [*Kite et al.*, 2013b]. Average modeled erosion rates are within or moderately exceed estimated erosion rates of Noachian and Hesperian terrains, 0.7–10 μm/yr, but are at the lower end of erosion rates from Earth, 2–100 μm/yr [*Golombek et al.*, 2006]. Having erosion and deposition rates falling within a reasonable range derived from the literature confirms the plausibility of our model assumptions.

In scenario 1, erosion and deposition are scaled equally to add and then remove the necessary materials over the specified time period. Of course, the time-averaged deposition could be more rapid than the time-averaged erosion or vice versa. In scenario 2, multiple sedimentation scenarios other than the simple D' parameterizations used (Table 1) are possible. We verified that a step function, e.g., from episodic volcanic ashfall or obliquity-driven sedimentation, produces a final form similar to the constant deposition case (scenario 2b). Multiple episodes of deposition and erosion could lead to generation of unconformities. The effects of these situations are accounted for by consideration of standard, minimum, and maximum diagenesis timescales. Under conditions of repeated episodes of erosion and fill, our estimates provided for temperature and TTI would be upper bounds because the sediments would persist for longer time periods with lower overburdens than modeled here.

4.2. Comparison of Model Results to Yellowknife Bay Mineralogy

Vaniman et al. [2014] identified trioctahedral smectites, anhydrite, bassanite, and magnetite at Yellowknife Bay in XRD data from the samples John Klein and Cumberland. Sedimentary rocks at the site show nodules and dark-toned raised ridges consistent with gas release during early sedimentary diagenesis and later, light-toned vein-fill from calcium-sulfate rich fluids [*Grotzinger et al.*, 2014; *Siebach and Grotzinger*, 2014; *Stack et al.*, 2014; *Léveillé et al.*, 2014]. Anhydrite and bassanite are the dominant Ca sulfates rather than gypsum. This could be a result of dehydration reactions at elevated temperature, but there is also a strong dependence of the reaction on water activity, which is unknown [*Vaniman et al.*, 2014]. Interestingly, XRD patterns indicate that the smectite interlayers in John Klein are collapsed, while those in Cumberland are held open, perhaps by metal hydroxides [*Bristow et al.*, 2015]. This, along with the gypsum veins, suggests an additional episode(s) of fluid interaction with the smectite clays after formation and that liquid water was present to enable diagenetic chemical reactions.

Given the observed lack of smectite conversion to other phases, our models for the temperatures experienced by the Yellowknife Bay sediments suggest that either (1) Yellowknife Bay was either never buried by $\gtrsim 2$ km of fill and mean Hesperian Mars surface temperatures were below zero or (2) water was unavailable during most of Yellowknife Bay's burial (Figure 7). Any scenario where Yellowknife Bay is buried under 5 km of fill (scenario 1) for long enough for temperatures to approach steady state (~300 kyr) leads to at least partial conversion of smectite to mixed layer clays and eventually to illite or chlorite if

water is available. With water and under scenario 1 of complete fill, conversion of smectites is predicted to be total in all except the minimum diagenesis timescale with cold early Mars case.

Scenarios where the crater is partially filled (scenarios 2a and 2b) do not predict any smectite to mixed layer clay conversion at Yellowknife Bay if average mean surface temperatures were substantially below 0°C because, even with burial of ~2 km, subsurface temperatures of the package of sedimentary rocks comprising the exposed outcrop do not exceed 0°C (Figures 5 and 6). In a warmer early Mars with $T_{surf} \geq 0$°C then partial to complete conversion of smectite to stable illite or chlorite forms would be expected at Yellowknife Bay, even with burial of only a few hundreds of meters, so long as water is available (Figure 7).

Thus, if deposition of Yellowknife Bay strata pre-dates Mount Sharp formation, a cold early Mars and slope wind model with relatively little burial is inferred because smectites remain as the most abundant phyllosilicate. However, the stratigraphic relationships between Yellowknife Bay sediments and other units are not entirely certain, and the deposit might instead represent a late-stage unit from Peace Vallis alluvial activity emplaced atop materials left behind during Mount Sharp's retreat [*Grotzinger et al.*, 2014]. There are smectite clays in the Gale Crater watershed which could have been delivered to the vicinity [*Ehlmann and Buz,* 2015]. Continued analysis of orbital and in situ data to understand contact relationships and the timing of sedimentation and clay formation is crucial. Moreover, these data highlight the importance of analysis of the mineralogy of Mount Sharp sedimentary rocks, where the stratigraphic relationships are clear, to determine the environmental history of Gale Crater deposits. Deposits inferred to be part of Mount Sharp and at similar elevations to Yellowknife Bay exist at Pahrump Hills, the location of the rover at the time of this writing.

4.3. Implications for Pore Water/Groundwater Temperatures During Diagenesis

Baseline models show peak paleotemperatures experienced by sedimentary rocks along the MSL traverse would have been up to ~80°C under the slope wind model (scenario 2) and ~125°C for the complete fill model (scenario 1), assuming a warm Mars surface temperature and $k \sim 2$ W/(m K). The maximum temperature possible under any model assumptions is 225°C, reached with for >4 km of overburden, a low thermal conductivity of $k = 1$ W/(m °C), and the highest heat flow model assumed. Estimates are reduced by ~50°C for a cold Mars more like that today. With these relatively low temperatures, phases like prehnite, found in some locations on Mars [*Ehlmann et al.*, 2009, 2011; *Carter et al.*, 2013] are not predicted for Gale Crater, and any chlorite that might be present would have a relatively restricted compositional/structural range characteristic of the low temperatures [e.g., *Inoue et al.*, 2009; *Bourdelle et al.*, 2013].

An important caveat to the analyses of temperatures above is substantial advection of heat by groundwater. That is, under conditions of high permeability and abundant water, the volumetric flux of water through sedimentary rocks could be a major heat transfer mechanism. Temperatures experienced by a given packet of sediments would be lower than modeled here if the waters flowing through them were mainly surface sourced, e.g., relatively cold from snowmelt or surface bodies of water. However, if water flowing through a given packet of sediments were upwelling from greater depths, temperatures could be higher than modeled.

The latter should be considered because the heat from the Gale impact may have resulted in a locally enhanced geothermal gradient for up to a few hundred thousand years [*Abramov and Kring,* 2005; *Schwenzer et al.*, 2012], which could have raised the temperatures of all our scenarios, depending on timing of Mount Sharp construction versus Gale Crater formation. Future work might examine the effects of fluid flow on diagenesis and feedbacks between secondary mineral precipitation, dissolution, groundwater chemistry, and maintenance of permeability to support fluid transport [e.g., *Giles,* 1997] and couple such diagenesis models to impact cratering models [e.g., *Abramov and Kring,* 2005]. The presence of a local magmatic body would have a similar enhancement on local surface heat flux in Gale Crater, affecting Mount Sharp sediments. The discovery of mineral phases whose formation temperatures can be pinned to > 150–225°C would implicate an impact—or volcanic—heating scenario.

4.4. Predictions for Diagenesis Along the Lower Mount Sharp Traverse

As Curiosity continues its trek up Mount Sharp, continued collection of mineralogic and textural data will constrain whether paleotemperatures were higher or lower in Mount Sharp compared to Yellowknife Bay, whether the conversion of smectite to nonswelling clay minerals took place, and whether diagenetic

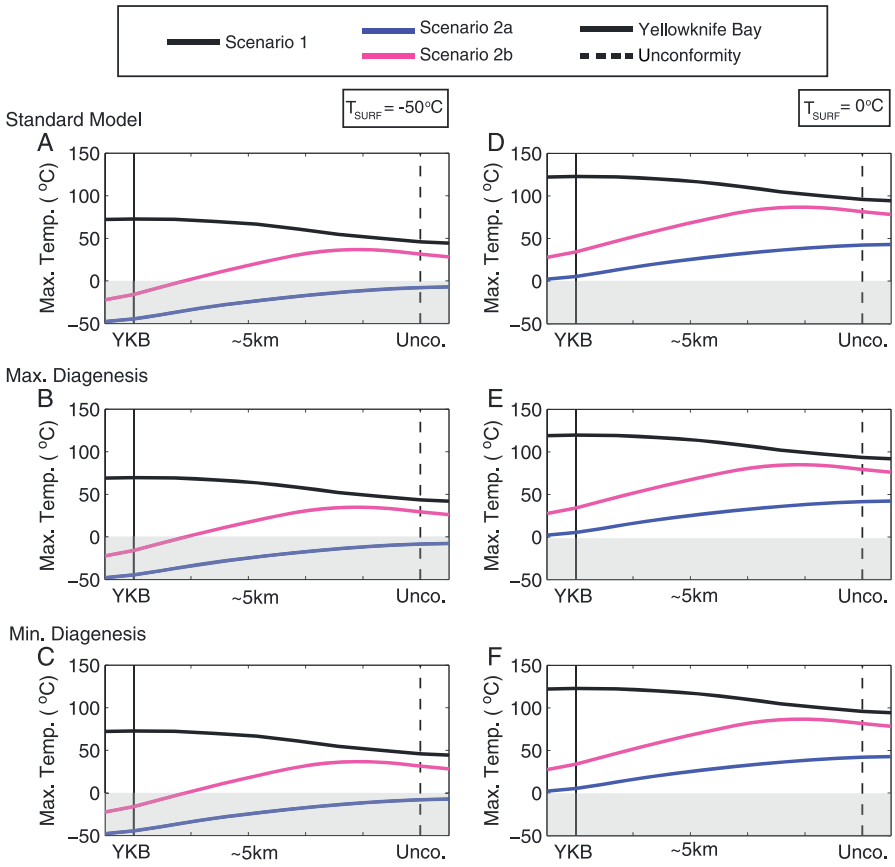

Figure 8. Maximum paleotemperatures experienced by sediments that currently crop out along MSL's traverse, considering different sedimentary scenarios and timescales for cold and warm early Mars.

conversions of other sulfate and silica phases may have occurred. Figure 8 provides maximum temperatures experienced by sedimentary rocks at locations between Yellowknife Bay and Mount Sharp, considering different depositional scenarios and different timescales. Importantly, even if absolute temperatures are affected by the factors discussed above, scenario 1 has a maximum paleotemperatures that decrease monotonically from Yellowknife Bay to the base of Mount Sharp, scenario 2a has an increasing maximum temperature along MSL's traverse, and scenario 2b has a peak maximum temperature at a current outcrop elevation of approximately −4 km in the Mars Orbiter Laser Altimeter (MOLA) elevation, near the hematite ridge.

What if lower Mount Sharp sedimentary units were deposited and then, after a substantial hiatus, the upper Mount Sharp sedimentary units were emplaced atop them? The latter may have occurred when waters for diagenesis were less available. Consequently, we performed two additional erosion/deposition tests for scenario 1. If the crater did not fill completely during the time windows considered but instead deposits only reached the highest of lower Mount Sharp units (maximum elevation of unit "lml" in *Thomson et al.* [2011], approximately −750 m), maximum temperatures and TTI's are similar to the ones described for the complete fill; e.g., for an early Mars surface temperature of −50°C, maximum temperature and value of TTI's are lowered by only 15°C and 3°C Gyr, respectively. If, instead, Gale Crater was only filled to the height of the unconformity (+1000 m above the present-day floor and similar to the altitude of the boxwork) [*Siebach and Grotzinger,* 2014] (Figure 4), less burial diagenesis would occur. The amount of overburden at Yellowknife Bay would be substantially smaller than in a complete-fill scenario 1 and comparable to the overburdens predicted in scenarios 2a and 2b. Notably, however, the pattern of diagenesis would differ: a partial fill scenario 1 would have evidence for diagenesis at Yellowknife Bay but none at all near the unconformity whereas scenario 2 would predict increasing diagenesis with height.

Given the evidence for water availability, i.e., fluid flow and diagnetic mineralization within sedimentary units investigated to date, these distinctive patterns provide testable constraints on the history of sedimentary deposition. If Gale Crater was completely filled then exhumed, diagenesis should decrease with distance up Mount Sharp, whereas incomplete fill under slope wind model scenarios would produce increased diagenesis toward the central part of the mound, i.e., as the rover climbs lower Mount Sharp. If temperature can also be discerned from diagenetic mineral assemblages determined by Curiosity, these constrain Hesperian surface temperatures, and thus paleoclimate, at Gale Crater.

5. Conclusions

Our sedimentation-thermal model predicts temperature as a function of time for two different scenarios for Mount Sharp evolution: (1) complete fill of Gale Crater followed by partial erosion and (2) partial fill dictated by slope winds. Determining maximum temperature experienced by sedimentary rocks and computation of time-temperature integrals provides a set of distinctive predictions for the extent of diagenesis, testable with MSL data. Our models produce erosion and deposition rates consistent with previously published Martian deposition and erosion estimates. Models show that if Gale Crater had been completely filled with sediments and pore waters were present, smectites in the sedimentary units of lower Mount Sharp would have been unstable and would have converted at least partially to other phyllosilicate phases. This suggests that either Yellowknife Bay was never buried by >2 km of overburden or there was insufficient water available for diagenesis of smectites, due to aridity, Hesperian mean annual surface temperatures well below zero, or impermeable rock.

Under a scenario of complete fill of Gale Crater, the rover should observe decreasing diagenesis as it climbs Mount Sharp, whereas a slope wind model predicts increasing diagenesis as the rover ascends through the Mount Sharp stratigraphic units. Minerals formed above 150–225°C are not predicted for any Gale Crater location in any burial diagenesis scenario. If these temperatures are derived from future mineral assemblages detected by Curiosity, this would implicate an additional source of heat, e.g., derived from the Gale Crater impact or local volcanism, or very inefficient heat transfer, e.g., caused by long-term burial by a porous, low thermal conductivity layer. Characterization of diagenetic textures and mineral assemblages observed by Curiosity as well as their spatial pattern along the rover traverse will allow testing sedimentation and heat flow models and thus reveal the paleoenvironmental and sedimentation histories of Gale Crater's Mount Sharp.

Acknowledgments
The data for this paper are available at NASA's PDS Geoscience Node. This work was partially funded by an MSL Participating Scientist grant to B.L.E. The Caltech Summer Undergraduate Research Fellowship program provided programmatic support to C.S.B. E.S.K. acknowledges support from a Princeton University Harry Hess fellowship.

References

Abramov, O., and D. A. Kring (2005), Impact-induced hydrothermal activity on early Mars, *J. Geophys. Res.*, *110*, E12S09, doi:10.1029/2005JE002453.

Anderson, R. C., and J. F. Bell III (2010), Geologic mapping and characterization of Gale Crater and implications for its potential as a Mars Science Laboratory landing site, *Mars*, *5*, 76–128, doi:10.1555/mars.2010.0004.

Beardsmore, G. R., and J. P. Cull (2001), *Crustal Heat Flow: A Guide to Measurement and Modelling*, Cambridge Univ. Press, Cambridge, U. K.

Bourdelle, F., T. Parra, C. Chopin, and O. Beyssac (2013), A new chlorite geothermometer for diagenetic to low-grade metamorphic conditions, *Contrib. Mineral. Petrol.*, *165*, 723–735.

Boyce, J. M., and H. Garbeil (2007), Geometric relationships of pristine Martian complex impact craters, and their implications to Mars geologic history, *Geophys. Res. Lett.*, *34*, L16201, doi:10.1029/2007GL029731.

Bridges, J. C., S. P. Schwenzer, R. Leveille, F. Westall, R. C. Wiens, N. Mangold, T. Bristow, P. Edwards, and G. Berger (2015), Diagenesis and clay mineral formation at Gale Crater, Mars, *J. Geophys. Res. Planets*, *120*, 1–19, doi:10.1002/2014JE004757.

Bristow, T. F., et al. (2015), The origin and implications of clay minerals from Yellowknife Bay, Gale Crater, Mars, *Am. Mineral.*, *100*(4), 824–836, doi:10.2138/am-2015-5077.

Carter, J., F. Poulet, J.-P. Bibring, N. Mangold, and S. Murchie (2013), Hydrous minerals on Mars as seen by the CRISM and OMEGA imaging spectrometers: Updated global view, *J. Geophys. Res. Planets*, *118*, 831–858, doi:10.1029/2012JE004145.

Ehlmann, B. L., and J. Buz (2015), Mineralogy and fluvial history of the watersheds of Gale, Knobel, and Sharp craters: A regional context for MSL Curiosity's exploration, *Geophys. Res. Lett.*, *42*, 264–273, doi:10.1002/2014GL062553.

Ehlmann, B. L., et al. (2009), Identification of hydrated silicate minerals on Mars using MRO-CRISM: Geologic context near Nili Fossae and implications for aqueous alteration, *J. Geophys. Res.*, *114*, E00D08, doi:10.1029/2009JE003339.

Ehlmann, B. L., J. F. Mustard, S. L. Murchie, J.-P. Bibring, A. Meunier, A. A. Fraeman, and Y. Langevin (2011a), Subsurface water and clay mineral formation during the early history of Mars, *Nature*, *479*, 53–60, doi:10.1038/nature10582.

Ehlmann, B. L., J. F. Mustard, R. N. Clark, G. A. Swayze, and S. L. Murchie (2011b), Evidence for low-grade metamorphism, hydrothermal alteration, and diagenesis on Mars from phyllosilicate mineral assemblages, *Clays Clay Miner.*, *590*(4), 359–377, doi:10.1346/CCMN.2011.0590402.

Fraeman, A., et al. (2013), A hematite-bearing layer in Gale Crater, Mars: Mapping and implications for past aqueous conditions, *Geology*, *41*(10), 1103–1106.

Garvin, J., S. Sakimoto, and J. Frawley (2003), Craters on Mars: Global geometric properties from gridded MOLA topography, *Sixth International Conference on Mars,* abs. #3277.

Giles, M. R. (Ed.) (1997), *Diagenesis: A Quantitative Perspective: Implications for Basin Modelling and Rock Property Prediction*, 526 pp., Kluwer Acad., Dordrecht, Netherlands.

Golombek, M., et al. (2006), Erosion rates at the Mars Exploration Rover landing sites and long-term climate change on Mars, *J. Geophys. Res.*, *111*, E12S10, doi:10.1029/2006JE002754.
Grant, J. A., et al. (2011), The science process for selecting the landing site for the 2011 Mars Science Laboratory, *Planet. Space Sci.*, *59*(11), 1114–1127.
Grotzinger, J. P., et al. (2012), Mars Science Laboratory mission and science investigation, *Space Sci. Rev.*, *170*(1–4), 5–56.
Grotzinger, J. P. (2014), A habitable fluvio-lacustrine environment at Yellowknife Bay, Gale Crater, Mars, *Science*, *343*(6169), 1242777, doi:10.1126/science.1242777.
Hahn, B. C., H. Y. McSween, and N. J. Tosca (2011a), Constraints on the stabilities of observed Martian secondary mineral phases from geothermal gradient models, in *Lunar and Planetary Science Conference*, vol. 42, p. 2340, The Woodlands, Tex.
Hahn, B. C., S. M. McLennan, and E. C. Klein (2011b), Martian surface heat production and crustal heat flow from Mars Odyssey Gamma-Ray spectrometry, *Geophys. Res. Lett.*, *38*, L14203, doi:10.1029/2011GL047435.
Harvey, H. R., J. H. Tuttle, and J. T. Bell (1995), Kinetics of phytoplankton decay during simulated sedimentation: Changes in biochemical composition and microbial activity under oxic and anoxic conditions, *Geochim. Cosmochim. Acta*, *59*(16), 3367–3377.
Hauck, S. A., II, and R. J. Phillips (2002), Thermal and crustal evolution of Mars, *J. Geophys. Res.*, *107*(E7), 5052, doi:10.1029/2001JE001801.
Inoue, A., A. Meunier, P. Patrier-Mas, C. Rigault, D. Beaufort, and P. Vieillard (2009), Application of chemical geothermometry to low-temperature trioctahedral chlorites, *Clays Clay Miner.*, *57*(3), 371–382.
Johnson, J. B., and R. D. Lorenz (2000), Thermophysical properties of Alaskan loess: An analog material for the Martian polar layered terrain?, *Geophys. Res. Lett.*, *27*(17), 2769–2772, doi:10.1029/1999GL011077.
Kalynn, J., C. L. Johnson, G. R. Osinski, and O. Barnouin (2013), Topographic characterization of lunar complex craters, *Geophys. Res. Lett.*, *40*, 38–42, doi:10.1029/2012GL053608.
Kargel, J. S., R. Furfaro, O. Prieto-Ballesteros, J. A. P. Rodriguez, D. R. Montgomery, A. R. Gillespie, G. M. Marion, and S. E. Wood (2007), Martian hydrogeology sustained by thermally insulating gas and salt hydrates, *Geology*, *35*(11), 975–978.
Kite, E. S., K. W. Lewis, M. P. Lamb, C. E. Newman, and M. I. Richardson (2013a), Growth and form of the mound in Gale Crater, Mars: Slope wind enhanced erosion and transport, *Geology*, *41*(5), 543–546.
Kite, E. S., A. Lucas, and C. I. Fassett (2013b), Pacing Early Mars river activity: Embedded craters in the Aeolis Dorsa region imply river activity spanned ≥(1–20 Myr), *Icarus*, *220*, 850–855.
Le Deit, L., E. Hauber, F. Fueten, M. Pondrelli, A. P. Rossi, and R. Jaumann (2013), Sequence of infilling events in Gale Crater, Mars: Results from morphology, stratigraphy, and mineralogy, *J. Geophys. Res. Planets*, *118*, 2439–2473, doi:10.1002/2012JE004322.
Lehmann, M. F., S. M. Bernasconi, and J. A. M. K. Barbieri (2002), Preservation of organic matter and alteration of its carbon and nitrogen isotope composition during simulated and in situ early sedimentary diagenesis, *Geochim. Cosmochim. Acta*, *66*(20), 3573–3584.
Léveillé, R. J., et al. (2014), Chemistry of fracture-filling raised ridges in Yellowknife Bay, Gale Crater: Window into past aqueous activity and habitability on Mars, *J. Geophys. Res. Planets*, *119*, 2398–2415, doi:10.1002/2014JE004620.
Lewis, K. W., and O. Aharonson (2014), Occurrence and origin of rhythmic sedimentary rocks on Mars, *J. Geophys. Res. Planets*, *119*, 1432–1457, doi:10.1002/2013JE004404.
Mackenzie, F. T. (Ed.) (2005), *Sediments, Diagenesis, and Sedimentary Rocks: Treatise on Geochemistry*, 2nd ed., vol. 7, 446 pp., Elsevier, Oxford, U. K.
Malin, M. C., and K. S. Edgett (2000), Sedimentary rocks of early Mars, *Science*, *290*(5498), 1927–1937.
Martínez, G. M., et al. (2014), Surface energy budget and thermal inertia at Gale Crater: Calculations from ground-based measurements, *J. Geophys. Res. Planets*, *119*, 1822–1838, doi:10.1002/2014JE004618.
McLennan, S. M., et al. (2014), Elemental geochemistry of sedimentary rocks at Yellowknife Bay, Gale Crater, Mars, *Science*, *343*, doi:10.1126/science.1244734.
Meunier, A. (2005), *Clays*, 472 pp., Springer, Berlin.
Milliken, R. E., and D. L. Bish (2010), Sources and sinks of clay minerals on Mars, *Philos. Mag.*, *90*, 2293–2308, doi:10.1080/14786430903575132.
Milliken, R. E., J. P. Grotzinger, and B. J. Thomson (2010), Paleoclimate of Mars as captured by the stratigraphic record in Gale Crater, *Geophys. Res. Lett.*, *37*, L04201, doi:10.1029/2009GL041870.
Milliken, R. E., R. C. Ewing, W. W. Fischer, and J. Hurowitz (2014), Wind-blown sandstones cemented by sulfate and clay minerals in Gale Crater, Mars, *Geophys. Res. Lett.*, *41*, 1149–1154, doi:10.1002/2013GL059097.
Morschhauser, A., M. Grott, and D. Breuer (2011), Crustal recycling, mantle dehydration, and the thermal evolution of Mars, *Icarus*, *212*(2), 541–558.
Nachon, M., et al. (2014), Calcium sulfate veins characterized by ChemCam/Curiosity at Gale Crater, Mars, *J. Geophys. Res. Planets*, *119*, 1991–2016, doi:10.1002/2013JE004588.
Parmentier, E. M., and M. T. Zuber (2007), Early evolution of Mars with mantle compositional stratification or hydrothermal crustal cooling, *J. Geophys. Res.*, *112*, E02007, doi:10.1029/2005JE002626.
Pelkey, S. M., B. M. Jakosky, and P. R. Christensen (2004), Surficial properties in Gale Crater, Mars, from Mars Odyssey THEMIS data, *Icarus*, *167*, 244–270.
Piqueux, S., and P. R. Christensen (2009), A model of thermal conductivity for planetary soils: 2. Theory for cemented soils, *J. Geophys. Res.*, *114*, E09006, doi:10.1029/2008JE003309.
Piqueux, S., and P. R. Christensen (2011), Temperature-dependent thermal inertia of homogeneous Martian regolith, *J. Geophys. Res.*, *116*, E07004, doi:10.1029/2011JE003805.
Rampe, E. B., et al. (2014), Evidence for local-scale cation-exchange reactions in phyllosilicates at Gale Crater, Mars, Clay Minerals Society Annual Meeting,Texas A&M, 17–21 May.
Robbins, S. J., and B. M. Hynek (2012), A new global database of Mars impact craters ≥1 km: 1. Database creation, properties, and parameters, *J. Geophys. Res.*, *117*, E05004, doi:10.1029/2011JE003966.
Ruedas, T., P. J. Tackley, and S. C. Solomon (2013), Thermal and compositional evolution of the Martian mantle: Effects of water, *Phys. Earth Planet. Inter.*, *220*, 50–72.
Ruiz, J., et al. (2011), The thermal evolution of Mars as constrained by paleo-heat flows, *Icarus*, *215*, 508–517.
Schwenzer, S. P., et al. (2012), Gale Crater: Formation and post-impact hydrous environments, *Planet. Space Sci.*, *70*, 84–95.
Scott, D. H., and M. G. Chapman (1995), Geologic and topographic maps of the Elysium paleolake basin, Mars, *U.S. Geol. Surv. Geol. Ser. Map I-2397*, scale 1: 5,000,000.
Siebach, K. L., and J. P. Grotzinger (2014), Volumetric estimates of ancient water on Mount Sharp based on boxwork deposits, Gale Crater, Mars, *J. Geophys. Res. Planets*, *119*, 189–198, doi:10.1002/2013JE004508.
Stack, K. M., et al. (2014), Diagenetic origin of nodules in the Sheepbed member, Yellowknife Bay formation, Gale Crater, Mars, *J. Geophys. Res. Planets*, *119*, 1637–1664, doi:10.1002/2014JE004617.

Thomson, B., et al. (2011), Constraints on the origin and evolution of the layered mound in Gale Crater, Mars using Mars Reconnaissance Orbiter data, *Icarus*, *214*(2), 413–432.

Tosca, N. J., and A. H. Knoll (2009), Juvenile chemical sediments and the long term persistence of water at the surface of Mars, *Earth Planet. Sci. Lett.*, *286*(3), 379–386.

Vaniman, D. T., et al. (2014), Mineralogy of a mudstone at Yellowknife Bay, Gale Crater, Mars, *Science*, *343*(6169), 1243480, doi:10.1126/science.1243480.

Velde, B. (1985), *Clay Minerals: A Physico-Chemical Explanation of Their Occurrence*, Dev. Sedimentol., vol. 40, 427 pp., Elsevier, New York.

Werner, S., and K. Tanaka (2011), Redefinition of the crater-density and absolute-age boundaries for the chronostratigraphic system of Mars, *Icarus*, *215*(2), 603–607.

Wray, J. J. (2012), Gale Crater: The Mars Science Laboratory/Curiosity rover landing site, *Int. J. Astrobiol.*, doi:10.1017/S1473550412000328.